

Article

Anisotropic Mechanical Response and Strain Localization of a Metallic Glassy-Fiber-Reinforced Polyethylene Terephthalate Fabric

Jie Li ¹, Bo Huang ^{1,*}, Jun Shen ², Jun Yi ¹ , Yandong Jia ¹, Rongjie Xue ³ and Gang Wang ¹

- ¹ Laboratory for Microstructures, Institute of Materials, Shanghai University, Shanghai 200444, China; jli@shu.edu.cn (J.L.); jxy305@gmail.com (J.Y.); yandongjia@shu.edu.cn (Y.J.); g.wang@i.shu.edu.cn (G.W.)
² College of Mechatronics and Control Engineering, Shenzhen University, Shenzhen 518060, China; junshen@szu.edu.cn
³ School of Materials Engineering, Jiangsu University of Technology, Changzhou 213001, China; xuerongjie@jsut.edu.cn
* Correspondence: huangb@shu.edu.cn; Tel.: +86-177-1783-6139

Abstract: Optimizing the mechanical properties of composites through microstructural design has been a long-standing issue in materials science. In this study, we reinforced a typical polymer, i.e., polyethylene-terephthalate-woven fabric, with a type of Fe-based metallic glassy fiber (MGF) with an extremely large Young's moduli. The MGF-reinforced fabrics, with three different fiber bundle orientations (0°, 45°, and 90°), were investigated by in situ electron-microscopy mechanical testing techniques in conjunction with a digital image correlation (DIC) technique. The fabrics exhibited a pronounced anisotropic mechanical response, and the associated characteristics were verified to depend on the fiber bundle orientation relative to the external load. Furthermore, localized strains near the intersections of the fiber bundles were found to be much higher than the global strain. It is confirmed that the restriction from warp to weft is the dominant factor influencing strain localization during deformation. Our results are enlightening for understanding the fracture mechanisms of composites.

Keywords: strain localization; metallic glassy fibers; digital image correlation; structural anisotropy



Citation: Li, J.; Huang, B.; Shen, J.; Yi, J.; Jia, Y.; Xue, R.; Wang, G. Anisotropic Mechanical Response and Strain Localization of a Metallic Glassy-Fiber-Reinforced Polyethylene Terephthalate Fabric. *Materials* **2021**, *14*, 5619. <https://doi.org/10.3390/ma14195619>

Academic Editor:
Danny V. van Hemelrijck

Received: 6 August 2021
Accepted: 17 September 2021
Published: 27 September 2021

Publisher's Note: MDPI stays neutral with regard to jurisdictional claims in published maps and institutional affiliations.



Copyright: © 2021 by the authors. Licensee MDPI, Basel, Switzerland. This article is an open access article distributed under the terms and conditions of the Creative Commons Attribution (CC BY) license (<https://creativecommons.org/licenses/by/4.0/>).

1. Introduction

Fabric composites are widely used as structural materials in our daily life and in other fields, such as the automobile and aero industries [1,2]. Their mechanical properties are one of the major concerns of scientific research. The application of fabric composites requires more a refined analysis that takes into account multiaxial failure behavior [3–5]. Existing studies provide different perspectives for understanding the influence of the fabric architecture and loading direction on the mechanical properties, and the damage behaviors of woven fabric composites [6–12]. Cai et al. [6,7] investigated the tensile properties of unidirectional and woven fabric glass/epoxy composites under on- and off-axis loading and found that the Tsai-Wu failure criterion is more accurate with a modified interaction coefficient under multiaxial stress conditions compared with the Tsai-Hill, Hoffman and Yeh-Stratton criteria. Zhou et al. [8] studied the damage evolutions of woven fabric composites with three different fabric architectures by monotonic and cyclic on- and off-axis tension tests. The results show that compacted yarns and the lower crimp ratio lead to less damage at the same loading strain and abrupt rupture. Guo et al. [9] revealed that bias yarns significantly enhance the in-plane shear modulus and strength of the multiaxial angle-interlocked woven composites, with the primary failure modes identified as fiber slippage, tow splitting, and interfacial debonding. Koohbor et al. [10] extracted carbon-fiber-reinforced composites at different off-axis angles, tested them in uniaxial tension, and correlated globally applied stress and locally developed deformation in the

materials. Zhai et al. [11] developed a coupled damage-plasticity model that describes the nonlinear off-axis tensile stress-strain relation of quasi-unidirectional E-glass fabric-reinforced polypropylene composites. Lu et al. [12] analyzed the on-axis uniaxial tensile behaviors and the tensile strengths of 2.5D woven fabric composites at different loading directions using a multiscale progressive damage finite element analysis simulating method. In spite of the extensive studies mentioned above, quantitative knowledge on the fracture mechanism of on- and off-axis loading, especially the local restraint effect relating to the microstructure, is still not fully established. Therefore, it is valuable to carry out more in situ analyses on the evolution of local strains before failure.

Apart from the uncertainty about the fracture mechanism, the mechanical properties (especially the strength) of fabric composites, mostly made up of polymers, also need to be further improved. With long-range disordered metallic bonding, metallic glasses (MGs) usually exhibit high strength and large toughness [13–15]. When the specimen is sufficiently small, it is difficult for the heterogenous nucleation of SBs, and the elastic limit and yielding strength of MGs increase [16,17]. An apparent small-size effect on compressive or tensile properties appears when the diameters of MG rods or fibers reach hundreds of nanometers [18,19]. With respect to the low dimensionality and excellent properties, it is intriguing to use metallic glass fibers (MGFs) as fillers to improve the mechanical performance of composites [20–22]. In addition, magnetically soft MGFs show giant magnetoimpedance (GMI) [23–25] and apparent permeability relaxation under electromagnetic excitations [26–28]. The MGF-reinforced composites can potentially be used as functional materials, such as electromagnetic interference filters and microwave absorbers [26–28].

Apart from the stress-strain curves and the fracture strength, other behaviors, such as local strain distribution and damage evolution, are also important for analysis and for modeling the anisotropic deformation and fracture behaviors of fabric composites. However, classical electrical resistance strain gauges do not have the adequate spatial resolution for the inhomogeneous local strain distributions. Digital image correlation (DIC), which has adequate spatial resolution and a full-field strain measurement, can be applied to determine local strain profiles, such as the maximum and minimum strain distribution [29–31]. The DIC technique has advantages in differentiating the slight variations of strain concentrations initiating damage caused by the local anisotropic microstructures. The main process of DIC technology is as follows: In order to capture the surface strain distributions during mechanical tests, artificial speckles were prepared on the surface of the specimen before loading. Then, several images were captured during the loading process by an image recording system, such as a CCD camera, optical microscope, or SEM. Finally, the local strains were computed through the correlation between these images and the initial image of the unloaded specimen using the software. The DIC technique has been applied to investigate the strain development and localization in, for example, anisotropic woven [32–34], laminate [35,36], and fiber- [37,38] and particle-reinforced composites [39,40].

In this paper, we explore the tensile properties of a polyethylene terephthalate fabric reinforced by soft magnetic Fe-based MGFs with structural anisotropy. Firstly, the tensile properties of the fabric specimens with three different loading directions are studied. Then, the strain-evolution processes are quantitatively analyzed with DIC technology. Finally, the restraint of warp on weft and the failure mechanisms of the fabric is discussed in detail.

2. Materials and Experimental Methods

The material under investigation in this work is an MGF-reinforced polyethylene terephthalate fabric, containing approximately 4% vol $\text{Fe}_{45.97}\text{Co}_{19.06}\text{Si}_{8.30}\text{B}_{15.23}\text{Ni}_{11.43}$ MGFs. The production of the MGFs was achieved through the glass-coated melt spinning method, and the glassy cover was removed using an aqueous HF solution [41]. The diameters of both the warp and weft bundles of the fabric were approximately 140 μm , and each fiber bundle contained one MGF and 16 polyester fibers (Figure 1a). The average diameter of the MGF was ~ 40 μm , and those of the fabric fibers were approximately 15 μm (see the inset

of Figure 1a). A schematic of the bundle structure in 3D view, and an overhead view, are shown in Figure 1b. It can be seen that a bundle of polyester fibers is surrounded by one MGF. The fabric weave pattern used in the experiment is 1/2 twill weave (shown in the inset of Figure 1c). For the tensile test, specimens with a dog-bone shape (Figure 1d) were cut from the original fabric in the 0° , 45° , and 90° direction with fiber bundle orientation angles. The schematic view is shown in Figure 1c. The tensile specimen is provided as Figure 1d, with guidelines for the dimensions of the specimen of the ASTM Standard E8 (2004). At least three specimens with the same fiber bundle orientation were prepared and tested to ensure the reproducibility of the test results.

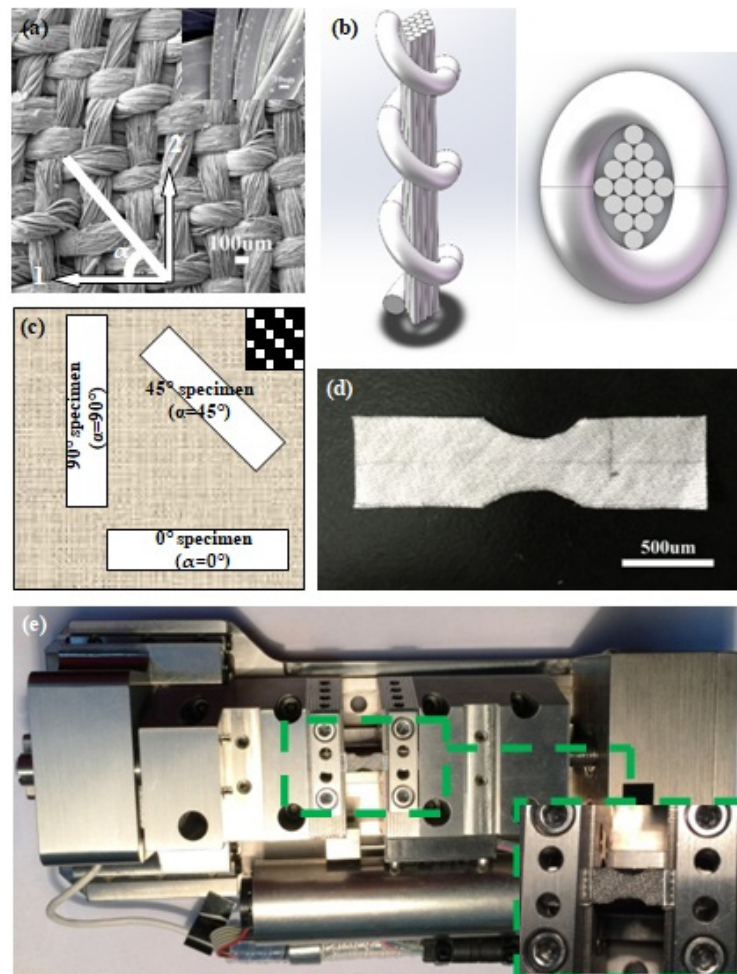


Figure 1. (a) Structure of the fabric, with the principal directions marked as 1 and 2. The image was captured by SEM, and the inset shows the detail of polyester fibers and an MGF; (b) A schematic of the bundle structure in 3D view and an overhead view; the orientation of the tensile specimens extracted from the original sheet is shown in (c), and the inset depicts the 1/2 twill fabric weave patterns; (d) A specimen used in the tensile experiment; (e) Miniature tension test frame with a composite specimen mounted.

The mechanical properties of MGF and polyester fiber were conducted by a loading stage (Gata Microtest Series) (shown in Figure 1e) with a gauge length of 10 mm and a strain rate of $1.7 \times 10^{-4} \text{ s}^{-1}$. To avoid slip during the tension test, the polymer fibers were bonded to a paper frame with a rhombic hole [42], and the MGF was enhanced by Ni electrodeposition at both ends [43].

A thin-layer gold film was deposited on the specimen surface via magnetron sputter coating to visualize the strain fields by DIC technology. Then, the composite specimens were mounted on a tensile test device for in situ deformation in a Apollo 300 SEM (CamScan,

Nottingham, UK). The loading stage (Gata Microtest Series), which is also used in tension tests on MGFs and polyester fibers, applied either by motor-driven or manually driven gears with a maximum tensile load of 2000 N, was installed inside the SEM chamber. Because there was no CCD conjunct with this scanning electron microscope, SEM images of the specimens were acquired in situ after each step of loading, and the digital speckle correlation images were acquired.

The load was applied monotonically at a rate of 0.4 mm min^{-1} , which corresponds to a strain rate of $6.7 \times 10^{-4} \text{ s}^{-1}$, using the displacement control mode. The elongation of composite at rupture is much higher than that of fibers, so we used a higher strain rate for the composite tension experiment than that of fibers for testing convenience. A grip length of 5 mm was marked at each end of the specimens, and four aluminum tabs were attached to the grip area at both ends of the specimens using an epoxy adhesive to minimize stress concentrations and the possible damage caused by the serrated steel grips of the tensile machine. During loading, consecutive surface images were recorded with a 1280×1024 -pixel array, and a pixel length of approximately $0.43 \text{ }\mu\text{m/pixel}$. A $540 \times 540 \text{ pixel}^2$ ($1.27 \times 1.27 \text{ mm}^2$)-calculated domain was located in the middle of the specimen. An image was obtained prior to loading, which served as the reference (undeformed) record. Sequential images were then analyzed with respect to this reference image using DIC, and the strain distributions at the different loads were then identified by a series of pronounced contour maps.

3. Results and Discussion

Uniaxial tension tests were carried out to examine the mechanical strength and elastic deformation of the fibers. Figure 2a shows the tension stress-strain curves of the MGF and polymer fiber. The deformation processes of the MGF and polymer fiber are similar and can be divided into two stages: elastic deformation and plastic deformation. The tension test results of MGF and polymer fibers are shown in Table 1. The elastic limit, the yield stress, and the elastic modulus of the MGF are 2.8%, 5.22 GPa, and 187 GPa, respectively, whereas the polymer fiber exhibits an elastic strain limit of 2.6% at a yield stress of 0.32 GPa, and the calculated elastic modulus is 12.34 GPa (shown in Table 1). The mixing rule [44] can be written as $\sigma_m^\alpha = V_p \sigma_p^\alpha + V_m \sigma_m^\alpha$, where σ_m^α , σ_p^α , and σ_m^α are the mechanical parameters of the composite, polyester fiber, and MGF, respectively, and V_p and V_m are the volume fraction of polyester fiber and MGF, respectively. In this fabric, V_p is 69%, and V_m is 31%. Compared with the polymer fiber, the MGF has almost the same elastic strain limit. However, the MGF exhibited a much higher yield stress and the elastic strain modulus, which enhances the mechanical properties of the fabric.

Table 1. The tension test results of the MGF and polymer fiber, i.e., Young's modulus (E), elastic limit (ϵ_e), yield stress (σ_y), maximum tension stress (σ_t), and plastic strain (ϵ_p).

Sample	E (GPa)	ϵ_e	σ_y (MPa)	σ_t (MPa)	ϵ_p
MGF	186.5	0.03	5.2	6.2	0.04
Polymer fiber	12.3	0.03	0.3	0.4	0.1

The tension stress-strain curves of specimens with three different fiber bundle orientations (0° , 90° and 45°) are plotted in Figure 2b–d. The stress-strain plots show a linear trend at the initial part of the curve, and then a nonlinear feature appears until the fabric failure. A possible cause of this deviation from linearity is local damage initiation; the damage process will be discussed later in this paper. For both the 0° and 90° specimens, the fracture stress is approximately 7 MPa. By comparing the measured stress of 0° and 90° specimens, it can be clearly observed that the strain of 0° specimens is smaller than that of 90° specimens at identical stress, indicating a stronger deformation resistance in 0° specimens. The maximum stress for the 45° specimen is less than 2 MPa, which demonstrates that the 45° specimen possesses the least stiffness and ductility among the three specimens.

These results suggest an anisotropic mechanical response, due to the strong sensitivity to the orientation of the fiber bundles. The elastic moduli E_x of woven composites at different loading directions can be expressed as [45]

$$E_x^{-1} = E_1^{-1} \cos^4 \theta + (G_{12}^{-1} - 2\nu_{12} E_1^{-1}) \sin^2 \theta \cos^4 \theta + E_2^{-1} \sin^2 \theta \quad (1)$$

where E_1 is longitudinal modulus, E_2 is transverse modulus, G_{12} is shear modulus, ν_{12} is Poisson's ratio, and θ is the off-axis loading direction. The failure-mode-independent and stress-based Tsai-Wu failure criterion [6,7] is applied to the off-axis tensile strength σ_x , and has the form [32]

$$F_{xx} \sigma_x^2 + F_x \sigma_x = 1, \quad (2)$$

where $F_{xx} = (X_t X_c)^{-1} \cos^4 \theta + (Y_t Y_c)^{-1} \sin^4 \theta + [S_{12}^{-2} - (X_t X_c Y_t Y_c)^{-1/2}] \sin^2 \theta \cos^2 \theta$ and $F_x = (X_t^{-1} - X_c^{-1}) \cos^2 \theta + (Y_t^{-1} - Y_c^{-1}) \sin^2 \theta$ with X_t/X_c is the uniaxial tensile/compressive strength in longitudinal direction, Y_t/Y_c is the uniaxial tensile/compressive strength in transverse direction, and S_{12} is the in-plane shear strength in the material coordinate system. As reported, a minimum value usually exists for E_x or σ_x , with θ equaling 45° based on Equation (1) or (2). The smallest stiffness and the fracture stress of the 45° specimen is consistent with the reported results.

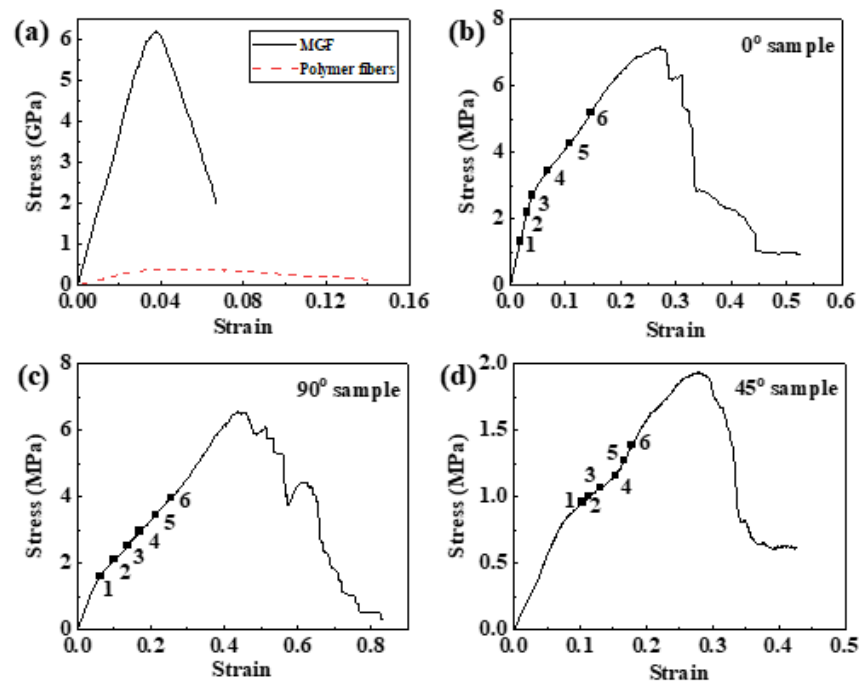


Figure 2. Tensile stress-strain curves of (a) MGF and polymer fiber, (b) 0° specimen, (c) 90° specimen, and (d) 45° specimen.

To explore the underlying failure mechanism microscopically, the corresponding specimens were investigated by SEM and the results are shown in Figure 3. For the 0° specimen, the fracture surface is almost perpendicular to the tension direction (as illustrated by the dashed line in the inset of Figure 3a). The fracture surface is an inclined plane for the 90° specimen (as illustrated in the inset of Figure 3c). In contrast, the 45° specimen is fractured at $\pm 45^\circ$ angled planes (as illustrated in the inset of Figure 3e). The SEM images of 0° and 90° specimens, randomly selected from the fracture surfaces, present similar behaviors, which both fracture throughout the specimen cross-section (Figure 3a,c). The straight fracture edges may be caused by the fiber pull-out mechanism. The SEM image of the 45° specimen, selected from the 45° angled plane of the conical fracture surface,

provides evidence of large shear deformation (Figure 3e). Additionally, the MGFs exhibit apparent necking after failure (Figure 3b,d,f).

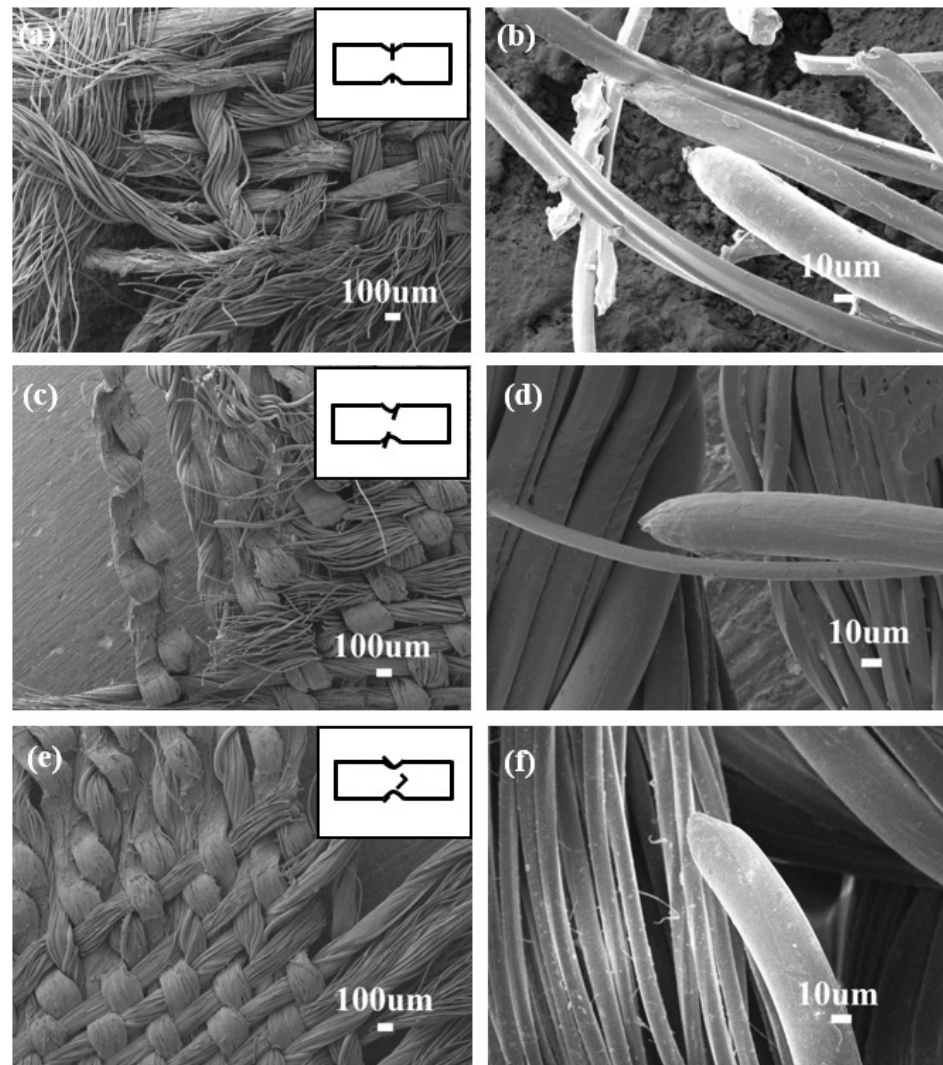


Figure 3. The SEM images of the fractured surface of (a) 0° specimen, (c) 90° specimen, and (e) 45° specimen with the insets showing the corresponding whole fractured surface schematically by the dashed lines. Lateral surface of the fractured MGFs for (b) 0° specimen, (d) 90° specimen, and (f) 45° specimen.

In order to explore the underlying mechanism of the two different failure modes under tension, we analyze the evolution of local strain fields obtained by the in situ DIC measurement. The SEM images of the 0° specimens before loading are shown in Figure 4a. On the basis of the undeformed state, strain-field development, including the ε_x fields along the loading direction (x -axis), the ε_y fields perpendicular to the loading direction (y -axis), and the shear-strain (γ_{xy}) fields, can be calculated. If the coordinate rotates by an arbitrary angle of θ , the local stresses can be expressed as [46]

$$\varepsilon'_x = \frac{1}{2} [(\varepsilon_x + \varepsilon_y) + (\varepsilon_x - \varepsilon_y)\cos 2\theta + \gamma_{xy}\sin 2\theta], \quad (3)$$

$$\varepsilon'_y = \frac{1}{2} [(\varepsilon_x + \varepsilon_y) - (\varepsilon_x - \varepsilon_y)\cos 2\theta - \gamma_{xy}\sin 2\theta], \quad (4)$$

$$\gamma'_{xy} = (\varepsilon_x - \varepsilon_y)\sin 2\theta + \gamma_{xy}\cos 2\theta. \quad (5)$$

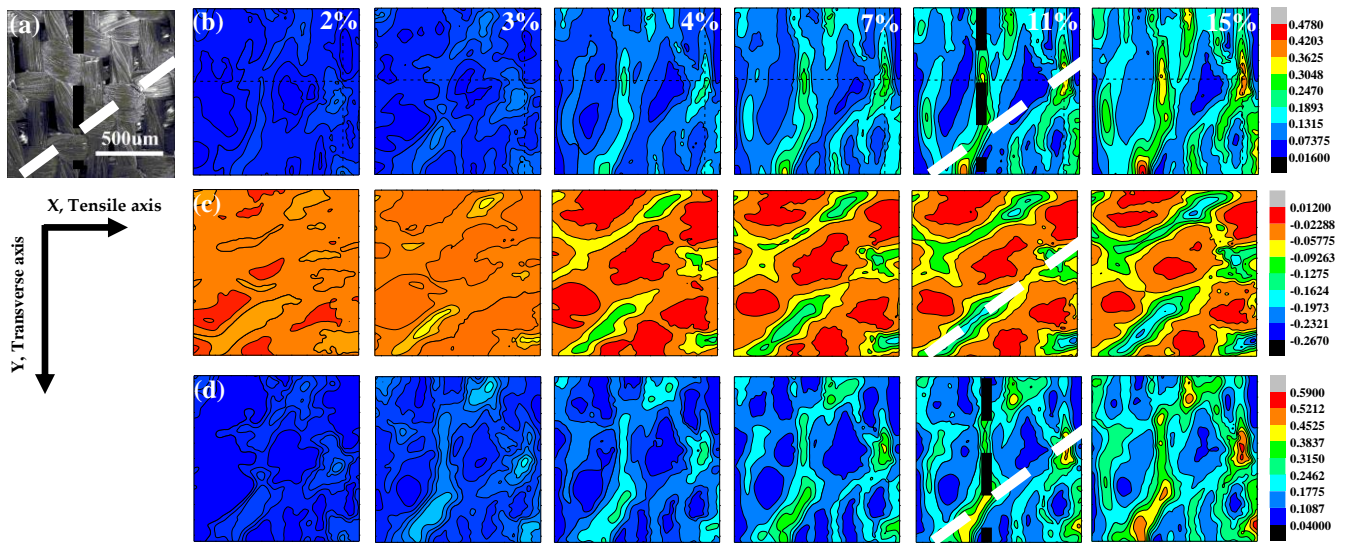


Figure 4. DIC images of strained 0° specimen: (a) speckle image of the 0° specimen before loading; (b) contour maps of the ε_{xmax} field; (c) contour maps of the ε_{ymax} field; (d) contour maps of the γ_{max} field.

From Equations (3)–(5), the express of the Mohr circle can be deduced as

$$\left[\varepsilon'_{x(y)} - \frac{1}{2}(\varepsilon_x + \varepsilon_y) \right]^2 + \left(\frac{\gamma'_{xy}}{2} \right)^2 = \frac{1}{4} [(\varepsilon_x - \varepsilon_y)^2 + \gamma_{xy}^2]. \quad (6)$$

From Equations (3)–(6), the local principle linear strains and corresponding rotation angles can be easily calculated as

$$\varepsilon_{x(y)max} = \frac{1}{2} \left[(\varepsilon_x + \varepsilon_y) \pm \sqrt{(\varepsilon_x - \varepsilon_y)^2 + \gamma_{xy}^2} \right], \quad (7)$$

$$\theta_{xmax} = \frac{1}{2} \arctan \left(\frac{\gamma_{xy}}{\varepsilon_x - \varepsilon_y} \right), \quad (8)$$

$$\theta_{ymax} = \frac{1}{2} \arctan \left(\frac{\gamma_{xy}}{\varepsilon_x - \varepsilon_y} \right) + \frac{\pi}{2}. \quad (9)$$

The local principle shear strain and rotation angle can be determined as

$$\theta_{ymax} = \frac{1}{2} \arctan \left(\frac{\gamma_{xy}}{\varepsilon_x - \varepsilon_y} \right) + \frac{\pi}{2}, \quad (10)$$

$$\theta_{ymax(min)} = \frac{1}{2} \arctan \left(\frac{\varepsilon_x - \varepsilon_y}{\gamma_{xy}} \right) = \theta_{xmax} + \frac{\pi}{2}. \quad (11)$$

Therefore, the maximum local normal strains ε_{xmax} and ε_{ymax} , and the maximum local shear strain γ_{max} , can be calculated by Equations (7)–(11).

Figure 4b–d display the strain developments for the ε_{xmax} , ε_{ymax} , and γ_{max} of the 0° sample, with global tensile strains as 2%, 3%, 4%, 7%, 11%, and 15%, respectively. It can be observed that ε_{xmax} and γ_{max} both increase with the global strain. In the initial stage, when the global strain is less than 3%, there is no obvious strain concentration zone in the contour maps. In Figure 2b, the stress and strain are linearly related. When the global strain is more than 7%, the strain concentration zone becomes more and more obvious, and the stress has a nonlinear relation with the strain, as shown in Figure 2b. Furthermore, large strain-concentration striations are formed in the ε_{xmax} and γ_{max} strain fields that lie at an angle of $\sim 90^\circ$ or $\sim 35^\circ$ to the direction of the tension load (marked by the black and white dashed lines in Figure 4b,d). Moreover, ε_{ymax} decreases with the global strain, and

the local strain striations of small $\varepsilon_{y_{max}}$ lie at an angle of $\sim 35^\circ$ to the direction of the tension load (marked by the white dashed line in Figure 4c). Compared with the SEM image in Figure 4a, it can be observed that the local large $\varepsilon_{x_{max}}$ and γ_{max} striations locate at the warp and weft intersections or along the boundaries of the warp bundles, while the $\varepsilon_{y_{max}}$ striations locate only at the warp and weft intersections.

The SEM image of the 90° specimen before deformation is mapped in Figure 5a. Figure 5b–d show the strain developments for $\varepsilon_{x_{max}}$, $\varepsilon_{y_{max}}$, and γ_{max} of the 90° sample, with global tensile strains as 6%, 10%, 14%, 17%, 21%, and 25%, respectively. It can be seen that the global tensile strain values for the 90° specimen are different from the 0° specimen. The elongation at maximum force for the 0° specimen is less than 0.3, but for the 90° specimen, the elongation at maximum force is more than 0.4, as shown in Figure 2b,c. In order to obtain the whole evolution process of the strain concentration, different global tensile strain values are chosen for the 90° specimen. $\varepsilon_{x_{max}}$ and γ_{max} both increase with the global strain, and the strain concentration zone becomes more and more obvious. In addition, the stress has a nonlinear relation with strain accompanied by strain concentrating, shown in Figure 2c. It seems that the large local $\varepsilon_{x_{max}}$ and γ_{max} striations all locate at the middle of the warp and weft intersections (as marked by the dashed black line in Figure 5a,b,d). It is interesting that the $\varepsilon_{y_{max}}$ striations lie at an angle of $\sim 35^\circ$ to the direction of the tension load (marked by the white dashed line in Figure 5c).

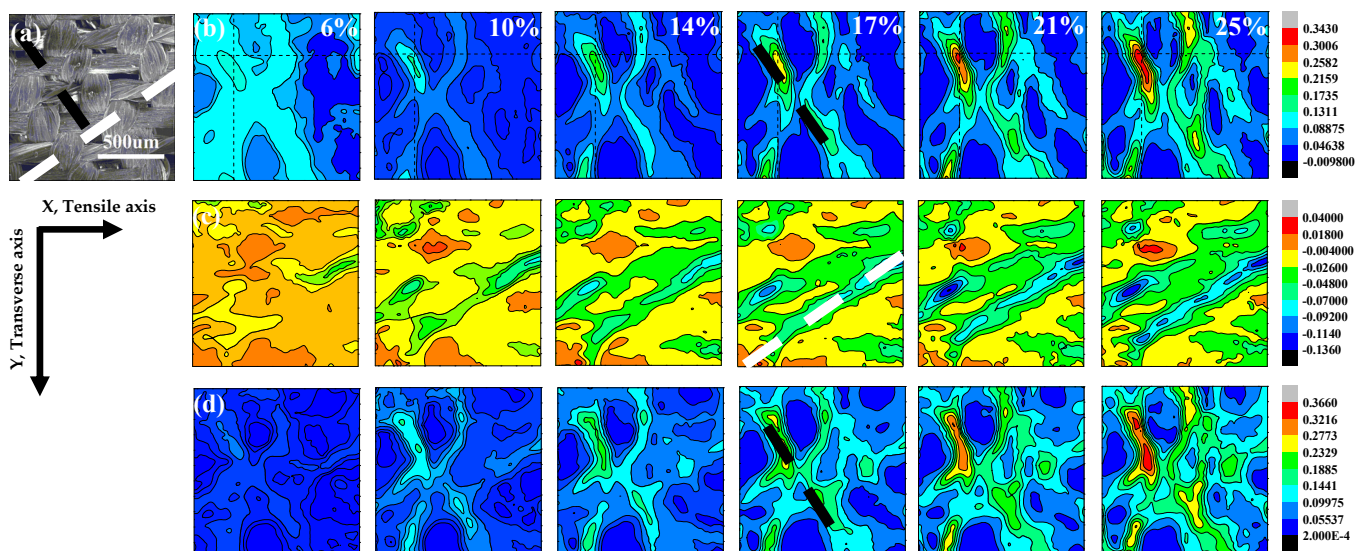


Figure 5. DIC images of strained 90° specimen: (a) Speckle image of the 90° specimen before loading. (b) Contour maps of the $\varepsilon_{x_{max}}$ field. (c) contour maps of the $\varepsilon_{y_{max}}$ field. (d) contour maps of the γ_{max} field.

Similarly, the SEM image of the 45° specimen before deformation is illustrated in Figure 6a. Figure 6b–d show the strain developments for $\varepsilon_{x_{max}}$, $\varepsilon_{y_{max}}$, and γ_{max} of the 45° sample, with the global tensile strains as 10%, 11%, 13%, 15%, 17%, and 18%, respectively. The $\varepsilon_{x_{max}}$ and γ_{max} concentrations are both isolated in the center of the specimen, and there are many overlapping regions of the two strain-concentration fields. With the emergence of strain concentration regions, the stress shows a nonlinear relation with strain (Figure 2d). However, the strain-concentration striations are observed in the $\varepsilon_{y_{max}}$ field at an angle of 12° to the direction of the tension load, which is fitted to the line of the adjacent warp and weft intersections (marked as a white dashed line in Figure 6a,c).

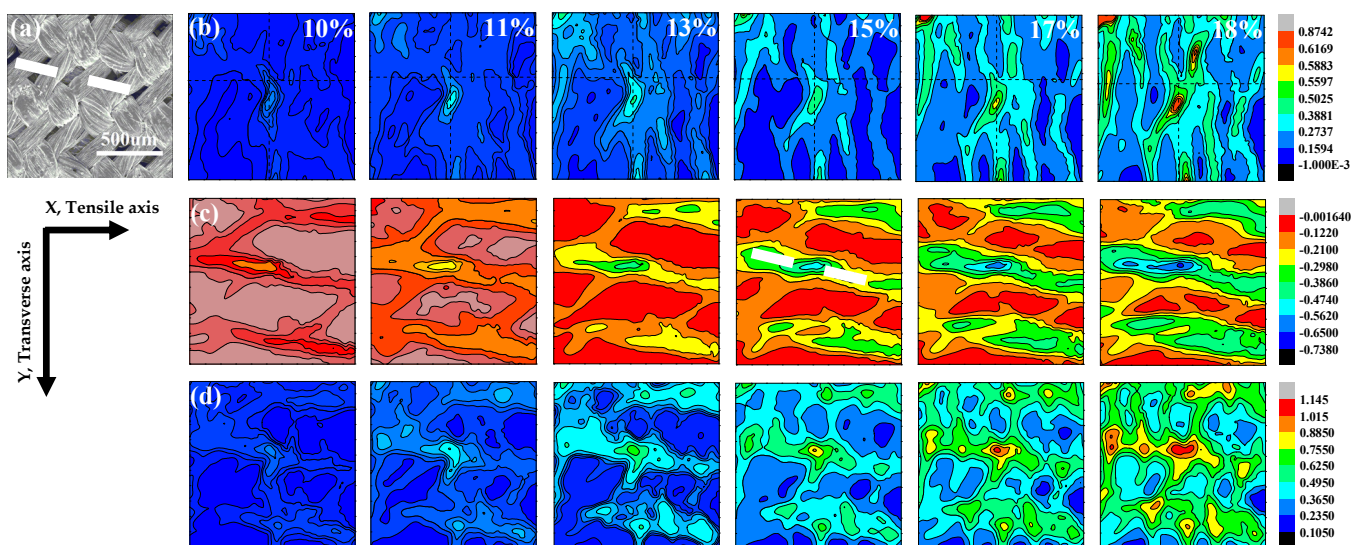


Figure 6. DIC images of strained 45° specimen. (a) Speckle image of the 45° specimen before loading. (b) Contour maps of the ε_{xmax} field. (c) Contour maps of the ε_{ymax} field. (d) Contour maps of the γ_{max} field.

To further characterize the development of strain localization with global strain, the distribution profiles of the ε_{xmax} values at different global strains for the three specimens on the principal stress plane, i.e., along the fine dash lines (x -axis) and dot lines (y -axis) in Figures 4–6, are displayed in Figure 7. For the 0° and 90° specimens, all of the ε_{xmax} along the x -axis and y -axis increases when the global strain increases (Figure 7a–d). Moreover, the maxima and minima of the ε_{xmax} periodically emerges along the x -axis (Figure 7a,c) when the global strain increases, but the maximum of ε_{xmax} only presents at the middle along the y -axis (Figure 7b,d). The peaks in Figure 7 correspond to the strain-concentrated regions along the dashed lines in Figures 4b, 5b, and 6b, which locate around the warp and weft intersections. The fiber bundles are perpendicular, or parallel, to the load direction in both of the 0° and 90° specimens. When the tensile load increases, the cross-section of the specimen decreases gradually, which results in the restraint of warp on weft at the warp and weft intersections and leads to strain localization behaviors. For the 0° and 90° specimens, the fiber bundles parallel to the tensile axis are under an isostrain condition [39] at lower global strain. It is shown in Figure 7a,c that the local strain values along both the x - and y -axes seem homogeneous at lower global strains, and most of these local strains are smaller than the global strain. However, with increasing load, the fiber bundles at the end of the specimen (near the grids) cannot generate an equal tensile strain with that of the middle part of the specimen because of the restraint of warp on weft. Moreover, when the global strain becomes larger, local strains fluctuate more apparently. This result suggests that the restraint of the warp bundles on the weft bundles increases with the global strain (Figure 7a–d). With the heterogeneous strain accumulation, the strain-concentration striations emerge along the x -axis (Figures 4b and 5b) where there are regions of periodic strain maxima or minima (Figure 7a,c). The different distances of periodic strain also reveal the different restraint effects of warp yarn on weft for the 0° and 90° specimens. Because of the striation distribution of the ε_{xmax} and γ_{max} fields, and the periodic strain maxima or minima along the x -axis, the nature of failure for both the 0° and 90° specimens can be explained by the fiber pull-out mechanism. Hence, the maximum stress of the 0° and 90° specimens are related to the number of transverse fiber bundles in the cross-section. Due to the same specimen dimensions and 1/2 twill woven pattern of the fabric, the two specimens have the same quantity of fiber bundles at the cross-sections and, thus, both the 0° and 90° specimens fracture at approximately 7 MPa (Figure 2b,c). Additionally, the weft gap of the 90° specimen, which lies between the adjacent warp and weft intersections, is longer than that of the 0° specimen, thus leading to a greater elongation of the 90° specimen (Figure 2b,c).

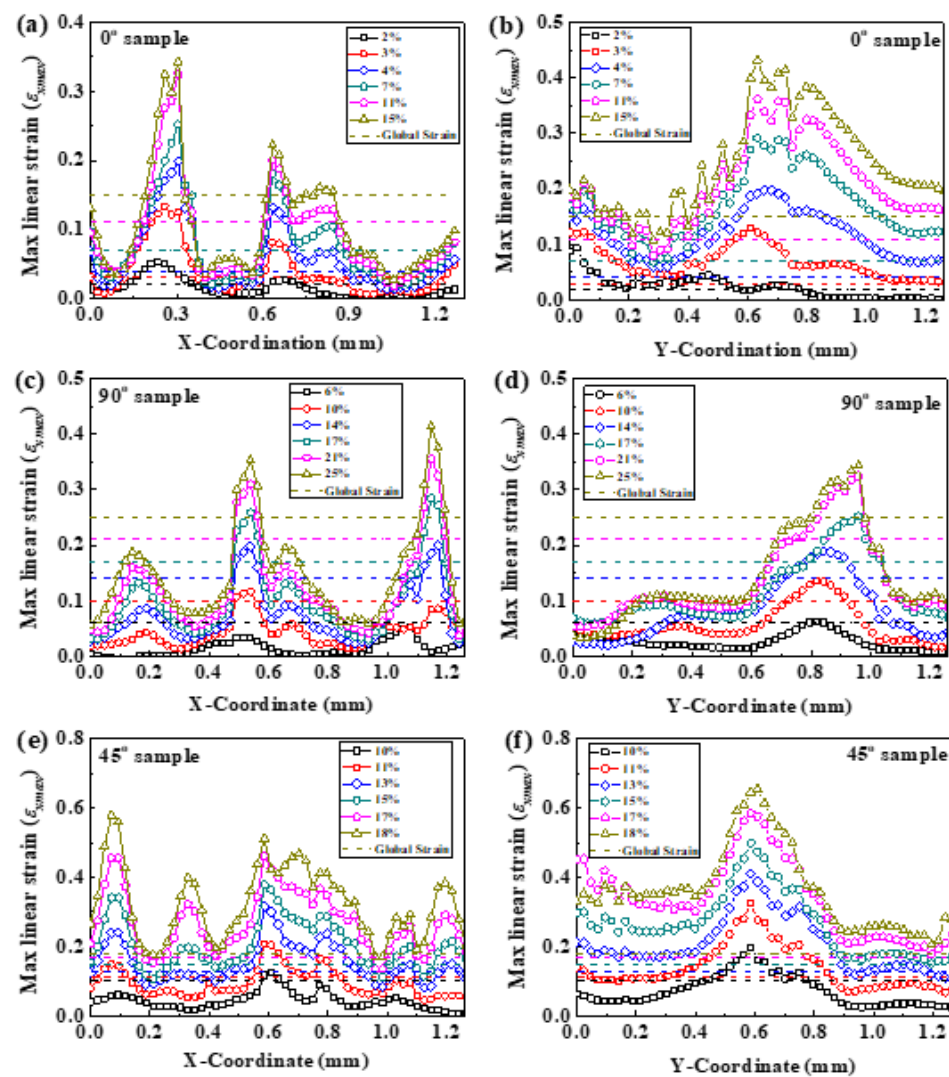


Figure 7. Profile of the distributions of the maximum ϵ_{xmax} values at different global strains of (a) 0° , (c) 90° , and (e) 45° specimens on the maximum shear stress plane, i.e., along the dash lines (x -axis), and at different global strains of (b) 0° , (d) 90° , and (f) 45° specimens along the dotted lines (y -axis) in Figures 4–6.

For the 45° specimen, the maxima and minima of ϵ_{xmax} periodically emerge along the x -axis (Figure 7e), but the maximum of ϵ_{xmax} only presents at the middle along the y -axis. The global strain increase in Figure 7f is similar to the above two specimens. In addition, all of ϵ_{xmax} along the x -axis and y -axis increases when the global strain increases, shown in Figure 7e,f. However, the fiber bundles of the 45° specimen are neither parallel nor perpendicular to the tensile axis but are oriented at $\pm 45^\circ$ angles with respect to the tensile axis. Thus, the number of warp and weft intersections along the x -axis is more than that of the 0° and 90° specimens (Figures 4a, 5a, and 6a), leading to more peaks of ϵ_{xmax} in Figure 7e related to the restraint effect. It is shown in Figure 7e,f that the local strain values along both the x - and y -axes seem homogeneous at lower global strains, and that most of these local strains are smaller than the global strain. However, with the tensile increasing, the cross-section of the specimen decreases, and the fiber bundles rotate towards the direction parallel to the load as the load increases gradually, which results in the restraint of warp on weft, and leads to strain localization behaviors. With the heterogeneous strain accumulation, the small separated strain-concentration regions emerge in the middle of the specimen (Figure 6d), leading to the maxima of ϵ_{xmax} presenting in the middle along the y -axis in Figure 7f. Owing to the different load responses of the

different components in the fabric, i.e., polyester fibers and MGFs, as well as the described fiber trellising phenomenon [47,48] under tension load, a shear strain would develop in the interfacial regions of different fiber bundles. Moreover, during the trellising shear deformation, the angle and interval between the weft and warp fiber bundles varies with the shear deformation. At an earlier stage of tension, smaller yarn gaps will introduce shear locking. However, with the increase in loading, the inter-yarn gap between the two adjacent parallel yarns becomes larger, which will make the fabric looser and will finally lead to a lower shear stiffness of the specimen. Therefore, the far-field load is shared between the polyester fibers and MGFs under a shear-type deformation with a significantly larger plastic deformation. For the fabric system studied here, this phenomenon becomes clear. High magnitudes of shear strain can result in damaging accumulation by void coalescence and result in an initial fracture in the center of the specimen [49]. In Figure 6d, the maximum of γ_{max} is isolated in the center of the specimen, and the specimen fails from that point. Thus, the 45° specimen exhibits a highly roughened conical fracture surface, as demonstrated in Figure 3e.

4. Conclusions

Based on in situ electron microscopy mechanical testing, in conjunction with DIC technology, the anisotropic mechanical response and strain localization of an MGF-reinforced fabric is investigated in this study. The following conclusions can be drawn:

- (1) The MGF is attributed to the enhanced mechanical properties of the fabric. The deformation processes of the MGF and polymer fiber are similar and can be divided into the elastic stage and the plastic stage. Although they had almost the same elastic strain limit, the MGF exhibited a much higher yield stress in the elastic strain modulus compared with the polymer fiber. According to the mixing rule, the MGF is beneficial to the mechanical enhancement of fabric.
- (2) The restraint of warp yarn on weft in the process of deformation is verified to be beneficial to the strain localization, which is the main cause of the fracture for fabric. With the local strain accumulation, the strain-concentration regions emerge. For the 0° and 90° specimens, the fiber bundles are parallel or perpendicular to the tensile axis. With the global strain increasing, the cross-section of the specimen decreases, resulting in the restraint of warp yarn on weft, and leading to strain localization behaviors. Moreover, the strain-concentration striations appear at the warp and weft intersections or along the boundaries of the warp bundles. For the 45° specimen, fiber bundles rotate towards the direction parallel to the load as the load increases gradually, which bring about the restraint effect and strain localization, and some small, isolated regions locate in the center of the 45° specimen.
- (3) The orientation of the fiber bundles strongly affects the fracture mechanism of the fabric because of different local fracture mechanisms. For the 0° and 90° specimens, the strain-concentration striations expose the fiber pull-out mechanism with straight fracture edges, and the 45° specimen is confirmed to fracture by shearing with a rough conical fracture surface due to the small, separated strain-concentration regions and the fiber trellising effect.

Overall, this study provides novel insights into the restraint of warp yarn on weft during the deformation process and improves the understanding of the deformation process and fracture mechanisms of a twill fabric. Although these results only refer to a twill fabric, they still provide some contributions to the referred topic, for example, advancing the understanding of the synergetic effects that often arise in hybrid composites, and assisting in contributing to the safety and reliable design of composite structures.

Author Contributions: Investigation, data curation, experiments, J.L., B.H., J.Y.; formal analysis, J.L., B.H.; writing original draft, manuscript revision, J.L., B.H., J.S., J.Y., Y.J., R.X., and G.W.; resources, supervision, project administration, funding acquisition, B.H., J.Y., Y.J., and G.W. All authors have read and agreed to the published version of the manuscript.

Funding: National Nature Science Foundation (NSF) of China: 52001193, 51801083 and 51901122. Natural Science Foundation of Jiangsu Province: BK20181044.

Institutional Review Board Statement: Not applicable.

Informed Consent Statement: Not applicable.

Data Availability Statement: Data are available upon request to the corresponding author.

Conflicts of Interest: The authors declare no conflict of interest.

References

1. Huang, T.; Wang, Y.L.; Wang, G. Review of the mechanical properties of a 3D woven composite and its applications. *Polymer* **2018**, *57*, 740–756. [[CrossRef](#)]
2. Alexander, J.; Augustine, B.S.M.; Prudhuvi, S.; Paudel, A. Hygrothermal effect on natural frequency and damping characteristics of basalt/epoxy composites. *Mater. Today* **2016**, *3*, 1666–1671. [[CrossRef](#)]
3. Zhou, G.W.; Sun, Q.P.; Li, D.Y.; Meng, Z.X.; Peng, Y.H.; Zeng, D.; Su, X.M. Effects of fabric architectures on mechanical and damage behaviors in carbon/epoxy woven composites under multiaxial stress states. *Polym. Test.* **2020**, *90*, 106657. [[CrossRef](#)]
4. Wang, Y.J. Mechanical properties of stitched multiaxial fabric reinforced composites from manual layup process. *Appl. Compos. Mater.* **2002**, *9*, 81–97. [[CrossRef](#)]
5. Tableau, N.; Aboura, Z.; Khellil, K.; Laurin, F. Multiaxial loading on a 3D woven carbon fiber reinforced plastic composite using tensile-torsion test: Identification of the first damage envelope and associated damage mechanisms. *Compos. Struct.* **2019**, *227*, 111305. [[CrossRef](#)]
6. Cai, D.A.; Zhou, G.M.; Wang, X.P.; Li, C.; Deng, J. Experimental investigation on mechanical properties of unidirectional and woven fabric glass/ epoxy composites under off-axis tensile loading. *Polym. Test.* **2017**, *58*, 142–152. [[CrossRef](#)]
7. Cai, D.A.; Tang, J.; Zhou, G.M.; Wang, X.P.; Li, C.; Silberschmidt, V.V. Failure analysis of plain woven glass/epoxy laminates: Comparison of off-axis and biaxial tension loadings. *Polym. Test.* **2017**, *60*, 307–320. [[CrossRef](#)]
8. Zhou, G.W.; Sun, Q.P.; Meng, Z.X.; Li, D.Y.; Peng, Y.H.; Zeng, D.; Su, X.M. Experimental investigation on the effects of fabric architectures on mechanical and damage behaviors of carbon/epoxy woven composites. *Compos. Struct.* **2021**, *257*, 113366. [[CrossRef](#)]
9. Guo, Q.W.; Zhang, Y.F.; Guo, R.Q.; Sun, X.L.; Chen, L. Experimental and numerical study of in-plane shear properties and failure process of multiaxial 3D angle-interlock woven composites. *Compos. Struct.* **2021**, *261*, 113296. [[CrossRef](#)]
10. Koohbor, B.; Ravindran, S.; Kidane, A. A multiscale experimental approach for correlating global and local deformation response in woven composites. *Compos. Struct.* **2018**, *194*, 328–334. [[CrossRef](#)]
11. Zhai, Z.Y.; Jiang, B.Y.; Drummer, D. Strain rate-dependent mechanical behavior of quasi-unidirectional E-glass fabric reinforced polypropylene composites under off-axis tensile loading. *Polym. Test.* **2018**, *69*, 276–285. [[CrossRef](#)]
12. Lu, Z.X.; Zhou, Y.; Yang, Z.Y.; Liu, Q. Multi-scale finite element analysis of 2.5D woven fabric composites under on-axis and off-axis tension. *Comput. Mater. Sci.* **2013**, *79*, 485–494. [[CrossRef](#)]
13. Inoue, A. Stabilization of metallic supercooled liquid and bulk amorphous alloys. *Acta Mater.* **2000**, *48*, 279–306. [[CrossRef](#)]
14. Johnson, W.L. Bulk glass-forming metallic alloys: Science and technology. *MRS Bull.* **1999**, *24*, 42–56. [[CrossRef](#)]
15. Wang, W.H. The elastic properties, elastic models and elastic perspectives of metallic glasses. *Prog. Mater. Sci.* **2012**, *57*, 487–656. [[CrossRef](#)]
16. Jang, D.C.; Greer, J.R. Transition from a strong-yet-brittle to a stronger-and-ductile state by size reduction of metallic glasses. *Nat. Mater.* **2010**, *9*, 215–219. [[CrossRef](#)] [[PubMed](#)]
17. Yang, G.N.; Shao, Y.; Liu, C.T.; Yao, K.F. How does the structural inhomogeneity influence the shear band behaviours of metallic glasses. *Philos. Mag.* **2020**, *100*, 1663–1681. [[CrossRef](#)]
18. Kumar, G.; Desai, A.; Schroers, J. Bulk metallic glass: The smaller the better. *Adv. Mater.* **2011**, *23*, 461–476. [[CrossRef](#)]
19. Jang, D.C.; Gross, C.T.; Greer, J.R. Effects of size on the strength and deformation mechanism in Zr-based metallic glasses. *Int. J. Plast.* **2011**, *27*, 858–867. [[CrossRef](#)]
20. Zhang, H.; Wang, C.D.; Zhang, Y.H.; Xie, J.X. Microwave absorbing properties of composites filled with glass-coated Fe₆₉Co₁₀Si₈B₁₃ amorphous microwire. *Mater. Sci. Eng. B* **2010**, *175*, 233–237. [[CrossRef](#)]
21. Qin, F.X.; Peng, H.X.; Prunier, C.; Brosseau, C. Mechanical-electromagnetic coupling of microwire polymer composites at microwave frequencies. *Appl. Phys. Lett.* **2010**, *97*, 153502. [[CrossRef](#)]
22. Marin, P.; Cortina, D.; Hernandez, A. High-frequency behavior of amorphous microwires and its applications. *J. Magn. Magn. Mater.* **2005**, *290*, 1597–1600. [[CrossRef](#)]
23. Phan, M.H.; Peng, H.X. Giant magnetoimpedance materials: Fundamentals and applications. *Prog. Mater. Sci.* **2007**, *53*, 323–420. [[CrossRef](#)]
24. Qin, F.X.; Peng, H.X. Ferromagnetic microwires enabled multifunctional composite materials. *Prog. Mater. Sci.* **2013**, *58*, 183–259. [[CrossRef](#)]
25. Moron, C.; Carracedo, M.T. Magneto-impedance effect in amorphous wires. *J. Mater. Process. Technol.* **2003**, *143*, 126–129. [[CrossRef](#)]

26. Li, D.R.; Lu, Z.C.; Zhou, S.X. Giant stress-impedance effect in amorphous and thermally annealed Fe_{73.5}Cu₁Nb₃Si_{13.5}B₉ ribbons. *Sens. Actuators A* **2003**, *109*, 68–71. [[CrossRef](#)]
27. Churyukanova, M.; Kaloshkin, S.; Shuvaeva, E.; Stepashkin, A.; Zhdanova, M.; Aronin, A.; Aksenov, O.; Arakelov, P.; Zhukova, V.; Zhukov, A. Non-contact method for stress monitoring based on stress dependence of magnetic properties of Fe-based microwires. *J. Alloys Compd.* **2018**, *748*, 199–205. [[CrossRef](#)]
28. Allue, A.; Corte-Leon, P.; Gondra, K.; Zhukova, V.; Ipatov, M.; Blanco, J.M.; Gonzalez, J.; Churyukanova, M.; Taskaev, S.; Zhukov, A. Smart composites with embedded magnetic microwire inclusions allowing non-contact stresses and temperature monitoring. *Compos. Part A* **2019**, *120*, 12–20. [[CrossRef](#)]
29. Dong, B.; Tian, L.; Pan, B. Tensile testing of carbon fiber multifilament using an advanced video extensometer assisted by dual reflector imaging. *Measurement* **2019**, *138*, 325–331. [[CrossRef](#)]
30. Denis, Y.; Guzman-Maldonado, E.; Morestin, F.; Hamila, N. Ultraviolet digital image correlation for molten thermoplastic composites under finite strain. *Exp. Mech.* **2019**, *59*, 439–451. [[CrossRef](#)]
31. Pan, B.; Li, K.; Tong, W. Fast, robust and accurate digital image correlation calculation without redundant computations. *Exp. Mech.* **2013**, *53*, 1277–1289. [[CrossRef](#)]
32. Yang, J.S.; Yang, X.G.; Zhu, H.X.; Shi, D.Q.; Chen, X.D.; Qi, H.Y. The effect of off-axis angles on the mesoscale deformation response and failure behavior of an rthotropic textile carbon-epoxy composite. *Compos. Struct.* **2018**, *206*, 952–959. [[CrossRef](#)]
33. Yu, L.P.; Pan, B. Experimental study of tensile properties and deformation evolutions of 2D and 2.5D woven SiO_{2f}/SiO₂ composites using single-camera stereo-digital image correlation. *Compos. Struct.* **2018**, *200*, 589–598. [[CrossRef](#)]
34. Koohbor, B.; Ravindran, S.; Kidane, A. Meso-scale strain localization and failure response of an orthotropic woven glass-fiber reinforced composite. *Compos. Part B* **2015**, *78*, 308–318. [[CrossRef](#)]
35. Pankowa, M.; Justusson, B.; Riosbaas, M.; Waas, A.M.; Yen, C.F. Effect of fiber architecture on tensile fracture of 3D woven textile composites. *Compos. Struct.* **2019**, *225*, 111139. [[CrossRef](#)]
36. Zhou, W.; Zhao, W.Z.; Zhang, Y.N.; Ding, Z.J. Cluster analysis of acoustic emission signals and deformation measurement for delaminated glass fiber epoxy composites. *Compos. Struct.* **2018**, *195*, 349–358. [[CrossRef](#)]
37. Borstnar, G.; Gillard, F.; Mavrogordato, M.N.; Sinclair, I.; Spearing, S.M. Three-dimensional deformation mapping of Mode I interlaminar crack extension in particle-toughened interlayers. *Acta Mater.* **2015**, *103*, 63–70. [[CrossRef](#)]
38. Szebenyi, G.; Hliva, V. Detection of delamination in polymer composites by digital image correlation-experimental test. *Polymers* **2019**, *11*, 523. [[CrossRef](#)]
39. Bie, B.X.; Huang, J.Y.; Su, B.; Lu, L.; Fan, D.; E, J.C.; Sun, T.; Fezzaa, K.; Qi, M.L.; Luo, S.N. Dynamic tensile deformation and damage of B4C-reinforced Al composites: Time-resolved imaging with synchrotron x-rays. *Mater. Sci. Eng. A* **2016**, *664*, 86–93. [[CrossRef](#)]
40. Nayak, S.; Das, S. Spatial damage sensing ability of metallic particulate-reinforced cementitious composites: Insights from electrical resistance tomography. *Mater. Des.* **2019**, *175*, 107817. [[CrossRef](#)]
41. Chiriac, H.; Ovari, T.A. Amorphous glass-covered magnetic wires: Preparation, properties, applications. *Prog. Mater. Sci.* **1996**, *40*, 333–407. [[CrossRef](#)]
42. Hussain, I.; Tong, X.; Wang, G.; Wang, J.G.; Yi, J.; Zhang, D.S.; Zhai, Q.J. Cooling rate-dependent yield behavior of metallic glass wires. *Mater. Sci. Eng. A* **2017**, *683*, 236–243. [[CrossRef](#)]
43. Hussain, I.; Jiang, Y.Y.; Jia, Y.D.; Wang, G.; Zhai, Q.J.; Chan, K.C.; Yi, J. Tensile behavior of Cu-coated Pd₄₀Cu₃₀Ni₁₀P₂₀ metallic glassy wire. *Sci. Rep.* **2018**, *8*, 5659. [[CrossRef](#)] [[PubMed](#)]
44. Lichtenecker, K. Dielektrizitätskonstante natürlicher und künstlicher Mischkörper. *Phys. Z.* **1926**, *27*, 115–158.
45. Cho, J.; Fenner, J.; Werner, B.; Daniel, I.M. A constitutive model for fiber-reinforced polymer composites. *J. Compos. Mater.* **2010**, *44*, 3133–3150. [[CrossRef](#)]
46. Atkin, R.J.; Fox, N. *An Introduction to the Theory of Elasticity*; Longman: London, UK, 1980.
47. Koohbor, B.; Ravindran, S.; Kidane, A. Meso-scale study of non-linear tensile response and fiber trellising mechanisms in woven composites. *J. Reinf. Plast. Comp.* **2016**, *35*, 986–995. [[CrossRef](#)]
48. Godara, A.; Raabe, D. Influence of fiber orientation on global mechanical behaviour and mesoscale strain localization in a short glass-fiber-reinforced epoxy polymer composite during tensile deformation investigated using digital image correlation. *Compos. Sci. Technol.* **2007**, *67*, 2417–2427. [[CrossRef](#)]
49. Xue, P.; Cao, J.; Chen, J.L. Integrated micro/macro-mechanical model of woven fabric composites under large deformation. *Compos. Struct.* **2005**, *70*, 69–80. [[CrossRef](#)]